Enhanced electrochemical performance of polyaniline and hyper-crosslinked porous polymer composite for advanced supercapacitor applications

Mohammed G. Kotp , Shiao-Wei Kuo [*]

Department of Materials and Optoelectronic Science, Center for Functional Polymers and Supramolecular Materials, National Sun Yat-Sen University, Kaohsiung, 80424, Taiwan

ARTICLE INFO

ABSTRACT

Supercapacitors are important for advanced energy storage because they have high power density, fast charge-discharge rates, and long cycle life. However, it is difficult to achieve both high energy density and good cycling stability. This study introduces a new composite material. It combines polyaniline (PANI) with a hyper-crosslinked porous polymer (HCP) that includes sulfonyldianiline (SOAM) and cyanuric (Cy) blocks. The PANI@SOAM-Cy HCP composite has a high surface area and good porosity for ion transport and charge storage. PANI adds pseudocapacitance. Cyclic voltammetry (CV), galvanostatic charge-discharge (GCD), and electrochemical impedance spectroscopy (EIS) characterize the electrochemical properties. The PANI@SOAM-Cy HCP composite achieves specific capacitances of 678 F g^{-1} and 325 F g^{-1} at 1.0 A g^{-1} in a three-electrode setup and a symmetric coin cell, respectively. The coin cell reaches an energy density of 45.14 W h kg^{-1} at a power density of 500 W kg^{-1} and maintains 17.73 W h kg^{-1} at 10,000 W kg^{-1}. The composite also shows good cycling stability, keeping 81.89 % of its initial capacitance after 5000 cycles at 10 A g^{-1}.

1. Introduction

Supercapacitors have attracted much of interest over the past few years, thanks to their high-power density, quick charge-discharge capabilities, and long cycle life, underlining their potential as alternatives for various energy storage systems [1]. However, it is still the difficulty in attaining high energy density besides preserving outstanding power density and cycling stability [2–5]. There are frequently issues with specific capacitance and long-term stability with conventional materials utilized in supercapacitors, such as active carbon or oxides of transition metals [6]. Hence, it becomes essential to create new electrode materials which may surpass beyond these constraints [7–9].

The prominent conducting polymer polyaniline (PANI) has been thoroughly studied for utilization in supercapacitors thanks to its high pseudocapacitance, convenience in manufacture, and durability in nature [10–12]. In spite of these benefits of PANI, the expansion and contraction of the chain throughout charge-discharge cycles induces poor cycling stability of those PANI-based supercapacitors, whereby in turn may trigger cracking and capacitance depletion [13–16]. For the purpose to tackle these shortcomings, chemists took a look at a number of ways to improve PANI's efficiency, such as integrating PANI with other materials to formulate composite frameworks [17,18]. Notably, PANI exceeds both Poly(3,4-ethylenedioxythiophene) (PEDOT) and (Polypyrrole) PPy in providing the highest specific capacitance due to its redox activity. While both PEDOT and PPy offer better mechanical flexibility, PANI stands out with its superior charge storage capabilities within composites [11].

Hyper-crosslinked polymers (HCPs) are crucial owing to functional and molecular attributes in an array of sophisticated technologies [19–21]. HCPs features by their extensive crosslinking, which derive a porous and stable network structure [22–24], thus for multiple purposes, such as adsorption, catalysis, and energy storage, considerable porosity they offer a significant surface area [25–28]. In terms of supercapacitors, HCPs have a number of notable benefits. Their large surface area provides functional ion adsorption and desorption, improving the electrochemical efficacy of electrode substrates [29–33]. With a diversity of pore diameters, the hierarchical pore design of HCPs assures swift ion flow and reduces resistance, facilitating charge-discharge processes and ultimate capacitance [34–36]. Since HCPs resist a wide range of chemical and temperature conditions, they

---

* Corresponding author.
*E-mail address:* kuosw@faculty.nsysu.edu.tw (S.-W. Kuo).

are the optimal option for harsh settings where dependable service is essential [37–39]. Furthermore, the flexibility of integrating HCPs with different chemical groups enables the customization of their features to fit specific use criteria [40].

The 4-[(4-aminobenzene)sulfonyl]aniline (SOAM) considers as crucial building block for supercapacitor electrodes, contributing effectively to the net activity of energy storage devices [41]. The sulfonyl groups in SOAM introduce high polarity and motivate an improved ionic conductivity, which is essential for dynamic charge transfer within supercapacitors [42,43]. Additionally, the aromatic structure of SOAM enhances the material's stability and its ability to form conjugated systems, which are essential for maintaining conductivity over long term turns. When incorporated into HCPs and combined with conductive polymers like PANI, SOAM blocks contribute to a synergistic effect that motivates the overall capacitance and durability of the nanocomposite [44]. The presence of SOAM in the supercapacitor's matrix ensures a robust framework that can endure the repeated swelling and shrinking cycles during charge-discharge processes, thus improving the device's long-term durability and effectiveness. This makes SOAM a valuable component in the design of advanced supercapacitors, aimed at achieving higher energy densities, faster charge-discharge rates, and longer operational lifespans.

By integrating PANI with an HCP incorporating SOAM and cyanuric blocks, we expect combination of the high conductivity and pseudocapacitive properties of PANI with the robust, porous nature of the HCP. Through harnessing the strongest aspects of both components, the innovative composition may create an electrode material that is extremely effective at storing energy while maintaining structural integrity. The incorporation of HCPs into this synthetic material may guarantee an improved electrochemical stability along with performance, rendering them promising for the advancement of future energy storage systems such as supercapacitors. To the best of our knowledge, there has been no previous study that has been conducted the pairing of PANI with HCP together to serve supercapacitor. The intent of this innovative integration is to investigate the potential features of coupling PANI's conductive and pseudocapacitive qualities plus the extensive surface area and hierarchical porosity of HCPs. The considerable crosslinking of HCPs is prevalent for producing a highly porous network that offers a large number of potential sites for ions adsorption and accelerates ion flow. On the other hand, PANI is esteemed for its strong pseudocapacitive properties and remarkable conductivity, both of which raise the total capacitance of the entire electrode. Thus, our objective is to combine the advantages of both materials to create a composite that performs better electrochemically by integrating PANI into HCP containing Cy and SOAM blocks. It is anticipated that this novel technique produces a material with uplevels of energy and power densities, along with exceptional turning stability and rate powers. The lack of earlier studies on this mix emphasizes how new our findings are and how they might drive the emergence of advanced energy storage devices.

In the current work, we designed the pristine PANI, SOAM-Cy HCP, and PANI@SOAM-Cy HCP nanocomposite (Scheme 1) and then fully characterized and discussed comparatively together using advanced instruments of FTIR, XPS, BET, TGA, TEM. Importantly, the PANI@SOAM-Cy HCP nanocomposite shows the intended molecular structure, albeit little surface area up to 38.31 m^2 g^{-1}, spherical
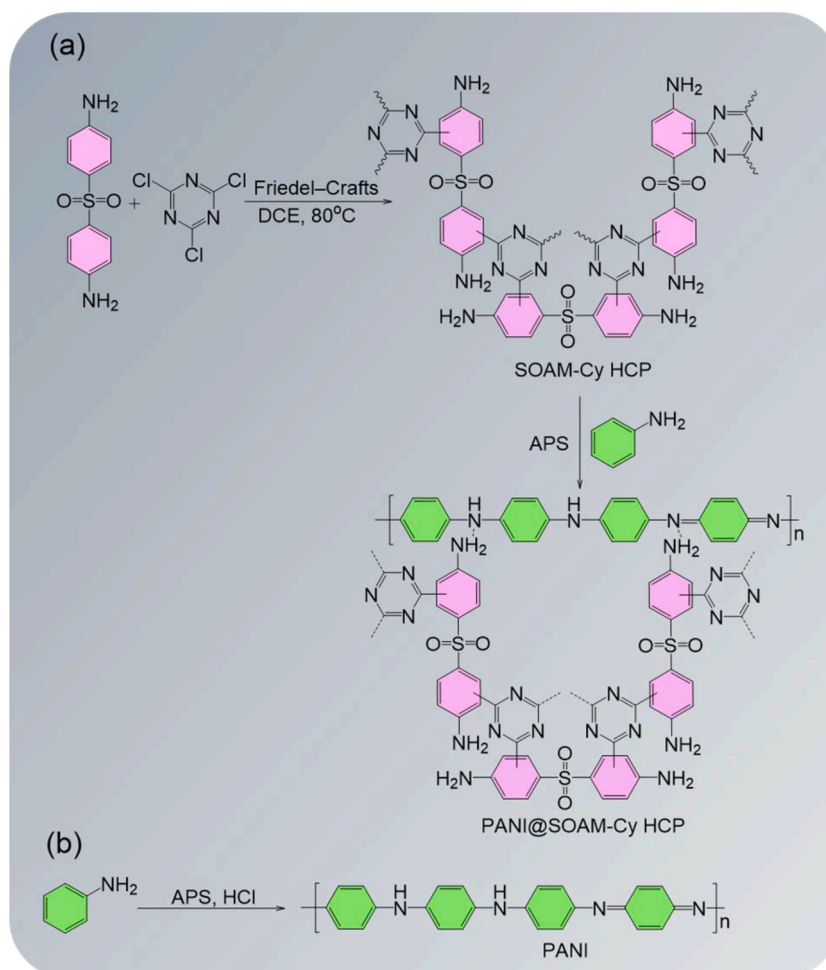
Scheme 1. (a)The synthesis design of the SOAM-Cy HCP, and PANI@SOAM-Cy HCP and (b) the polymerization of pristine PANI.

morphology, as well as higher thermal stability recording char yield up to 44 wt.%. At the meantime we investigated their electrochemical performance in a three-electrode system, plus symmetric configuration of a coin cell utilizing a variety of methods, such as cyclic voltammetry (CV), galvanostatic charge-discharge (GCD), and electrochemical impedance spectroscopy (EIS), to assess their capacitive behavior, cycling stability, and charge transfer resistance. Our results demonstrate that the PANI@SOAM-Cy HCP composite exhibits a significant improvement in particular capacitance, as well as energy and power densities up to 678.93 F g^{-1} and 94.27 Wh Kg^{-1} compared to the pristine PANI or SOAM-Cy HCP. Moreover, the PANI@SOAM-Cy HCP composite demonstrates outstanding cycling stability, retaining uplevels of specific capacitance and coulombic efficiency after 5000 cycles up to 81.89 %. The coin cell system integrated the PANI@SOAM-Cy HCP exhibits a particular capacitance of 325.00 F g^{-1} at current density of 1 A g^{-1}. Our study opens the door toward designing of forefront energy storage systems with better electrochemical properties and long-term durability by tackling the shortcomings with traditional PANI-based supercapacitors.

2. Experimental section

2.1. Synthesis of SOAM-Cy HCP

In a pyrex tube, cyanuric chloride (742 mg, 4.1 mmol) was dissolved in 15 mL of dichloroethane under 5 °C. After that, the 4,4′-sulfonyldianiline (1.49 g, 6.15 mmol) solved in 15 mL of DCE was stirred for 24 h under ambient temperature. Later, the Lewis acid of the AlCl$_3$ (10.5 μL, 0.012 mmol) was inserted prior to raising the temperature of the mixture to 100 °C under refluxing conditions for consecutive 3 days. The mixture was allowed to cool to RT then the precipitate was filtered as well rinsed successively with methanol, acetone, and THF then it was dried under evacuee at 60 °C to yield white color with a yield of 92 %.

2.2. Synthesis of polyaniline

Typically, 0.2 mol l^{-1} aniline and 0.25 mol l^{-1} APS were dissolved in 0.1 M HCl to prepare the standard PANI as reported et al., [45]. Typical PANI salt that had precipitated was collected onto filter paper and then vacuum-dried at 70 °C. To deprotonate PANI salt (PANI base), an excess of 0.1 mol l^{-1} ammonia was administered.

2.3. Synthesis of PANI@SOAM-Cy HCP

In the current study, we selected a 1:1 mass ratio aiming to balance PANI's pseudocapacitance with the HCP's porous network for optimal synergy between conductivity, ion transport, and structural stability. While higher PANI content could enhance conductivity, excessive loading risks pore blockage and reduced electrolyte accessibility, whereas higher HCP content might compromise conductivity despite improved porosity. Generally, an ultrasonicate device was used to disperse 0.5 g of SOAM-Cy HCP in 100 mL of 0.1 M HCl. Subsequently insertion of 0.5 g (37 mmol) of aniline. Ammonium peroxydisulfate (0.438 g, 1.9 mmol in 50 mL of 0.1 M HCl) was inserted after the mixture had been agitated for two hours and allowed to cool in an ice bath. It became apparent to let the aniline polymerize overnight. After centrifuging, the PANI@SOAM-Cy HCP salt nanocomposite (doped form) was re-dispersed in a 1 M HCl solution and centrifuged again. The PANI@SOAM-Cy HCP was immersed in 0.1 M ammonia solution to deprotonate it to the matching base (dedoped) form, which was then filtered and vacuum-dried at 70 °C.

3. Results and discussion

To design novel SOAM and Cy incorporated HCP we utilized the common *Friedel–Crafts* protocol in the presence of AlCl$_3$ as a Lewis acid. Notably, the amino group in SOAM is not directly involved in the

reaction with cyanuric chloride. Otherwise, the reaction occurs at the aromatic ring, which is the site of the acylation driving the SOAM-Cy HCP (Scheme 1). On the second step, we polymerized the aniline onto the surface of this SOAM-Cy HCP resulting the PANI@SOAM-Cy HCP composite (Scheme 1a). For clear visualization, we also polymerized the pure aniline separately (Scheme 1b) as previously reported [46,47]. The pristine PANI, SOAM-Cy HCP, and PANI@SOAM-Cy HCP have been physically characterized and compared utilizing those advanced techniques of FTIR, XPS, BET, TGA, SEM, and TEM. Moreover, their electrochemical performances have been investigated by those validated techniques of CV, GCD, and EIS with deep analyses.

3.1. FTIR profile

The PANI's FTIR record (Fig. 1a) reveals the N—H stretching vibration, which plays a role in the visible sign at 3450 cm^{-1}. Additionally, the C=C stretching patterns of the quinoid and benzenoid units assume responsibility for the bands at 1588 cm^{-1} and 1490 cm^{-1}, respectively. Further signs at 1382 cm^{-1} are caused by the C—N stretching vibration, 1299 cm^{-1} by the C—N stretching vibration of the 2nd arylamine, 1140 cm^{-1} by the C—H in-plane bending vibration, and 823 cm^{-1} by the out-of-plane C—H bending vibration of the para-disubstituted benzene ring. These data correspond closely with those released [48]. Throughout the FTIR track of the SOAM-Cy HCP, the stretching vibrations of such aromatic C—H signals are exhibited at wavenumbers of approximately 3026 cm^{-1} and at 1600 cm^{-1} points for aromatic C=C bonds. Moreover, such visible band at 1615 cm^{-1} (Figs. 1a) assumes the C=N bonds. Additionally, the stretching vibrations bond of S=O are visible at 1111 cm^{-1} [49].

Interestingly, the FTIR profile of the SOAM-Cy HCP considers the first evident for the successful crosslinking and connection of the SOAM-Cy HCP. For the PANI@SOAM-Cy HCP's nanocomposites, the bands at 1109 cm^{-1} verify that SOAM is present in this innovated nanocomposite. Further, the C—C of the stretching modes of the quinonoid and benzenoid units within the PANI chains are attributed to the signals at 1593 and 1499 cm^{-1}, respectively. Furthermore, the C—N stretching vibration in the (Q–B–Q) unit and the vibration of the 2nd arylamine are attributed to the signals at 1382 cm^{-1}. The SOAM-Cy HCP's absorption signs at 1111 cm^{-1} slightly moved to 1109 cm^{-1}, showing that the SOAM-Cy HCP's *S=O* units participated in the crosslinking that led to the creation of the PANI@SOAM-Cy HCP nanocomposite. Furthermore, the stretching vibration of N—H based PANI which is responsible for an apparent signal at 3450 cm^{-1} shifted to 3459 cm^{-1} also indicates that N—H units take part in this formation of the current nanocomposite. All together assume the hydrogen bonding between the SOAM-Cy HCP, and PANI deriving the successful formation of the PANI@SOAM-Cy HCP composite. The solid-state ^{13}C NMR of those as-designed PANI, SOAM-Cy HCP, and PANI@SOAM-Cy HCP nanocomposite displays characteristic signals in the range from 143 to 114 ppm, which reveals to the aryl C=C and C=C—H carbons (Fig. 1b). Moreover, those SOAM-Cy HCP and PANI@SOAM-Cy HCP composite exhibits an additional peak at 153 ppm, revealing the C-S units of the SOAM molecules (Fig. 1b).

3.2. XPS measurements

To deeply illustrate the fundamental structure of PANI, SOAM-Cy HCP, and PANI@SOAM-Cy HCP surfaces along with their respective electronic configurations, we utilized the XPS instrument. Within the current study, the PANI solid's chemical pattern is confirmed by clearly visible high resolution XPS signals of C1s, N1s, and O1s (Fig. 2 and Fig. S1). A total of three bands arises by the deconvolution of the C1s pulse from the PANI sample (Fig. 2a). These bands represent various forms of carbon, including sp^2 carbon particles (C=N, 285.5 eV), sp^2 carbons linked oxygen (C—O, 284.8 eV), and sp^2 carbon (C=C, 284.1 eV). Otherwise, the N1s response of the pristine PANI shows a single-molecule peak at 399.08 eV imply for C—N-H units (Fig. 2b) [50–52].
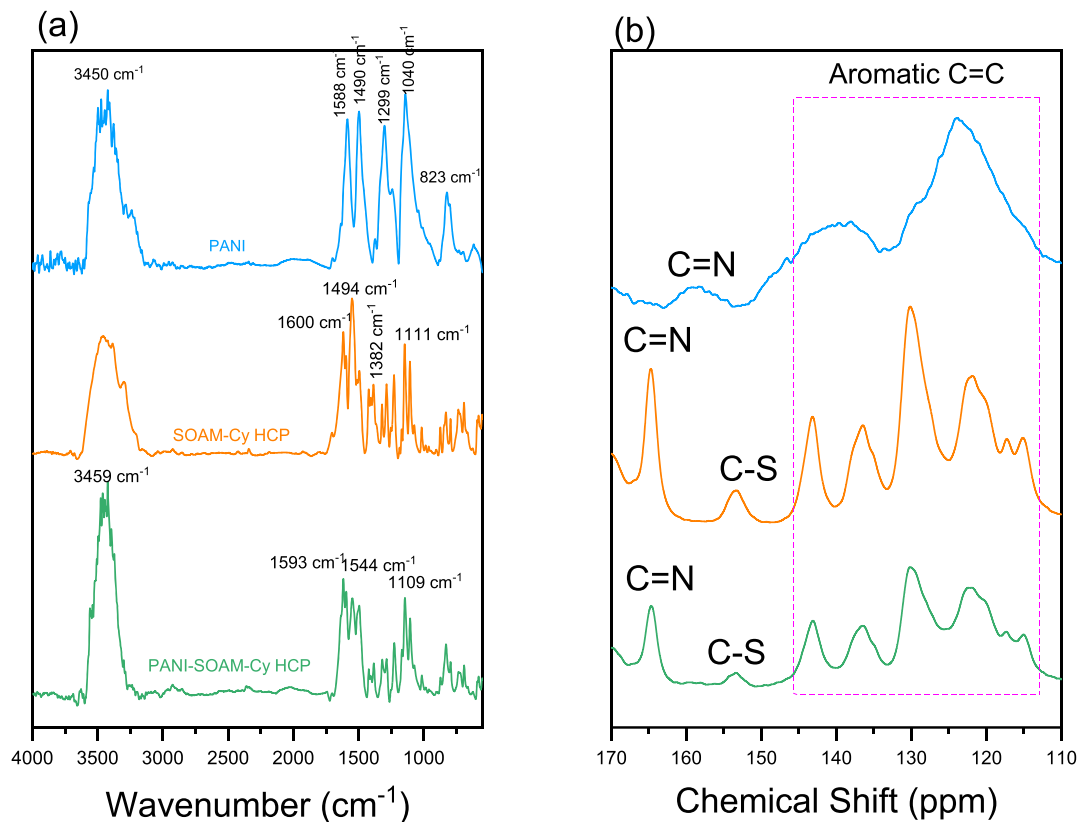
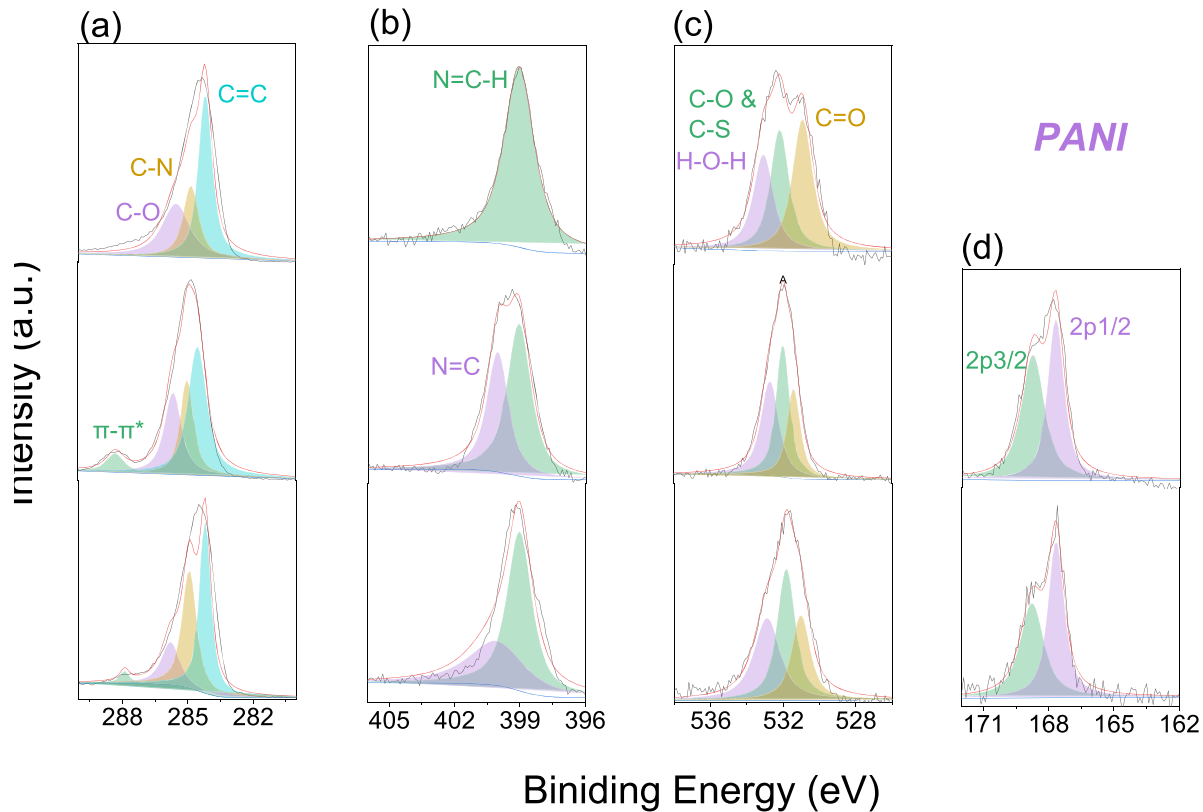**Fig. 1.** (a) FTIR spectra and (b) solid state NMR spectra of PANI, SOAM-Cy HCP, and PANI@SOAM-Cy HCP.

Fig. 2. HRXPS of C1s (a), N1s (b), O1s (c), and S2p (d) incorporated those of PANI (top), SOAM-Cy HCP (middle), and PANI@SOAM-Cy HCP (down) composite.

Notably, the surface of PANI can absorb moisture (H₂O) and other oxygen-containing contaminants from the environment [53]. These adsorbed species can contribute to the oxygen signal observed in XPS measurements [33]. Even trace amounts of oxygen from atmospheric exposure can result in detectable XPS signals [54]. The PANI shows trioxides at 533.08, 532.18, and 530.92 eV (Fig. 2c), which stand for hydrated oxygen (H—O-H), C—O, and $C = O$ species respectively. Considering the innovated SOAM-Cy HCP, the chemical as well as electronic properties of the compounds can be inferred from the XPS patterns.

As earlier mentioned, the C1s signs for the PANI divided into three sections including the sp² carbons (C—N, 285.5 eV), sp² carbons bonded to hydroxyl oxygen (C—O or C-S, 284.82 eV), sp² carbon (C═C, 284.15 eV) in addition to very broad peak at 287.9 eV for the π-π*. Significantly, the C 1 s state is unable to accurately discriminate between the C–O, C–S, and C–S–H bonds since their close binding energies (Fig. 2a). Furthermore, the N1s of the SOAM-Cy HCP deconvolutes into couple bands at 400.06 eV and 399.08 eV correspond to N═C of the triazine unit, and C—N-H of amino groups based the SOAM subunits (Fig. 2b). Furthermore, the O1s deconvolution of the SOAM-Cy HCP shows the similar three oxides of PANI including an impalpable shift of their binding energies at 533.08, 532.18, and 530.92 eV (Fig. 2c), which stand for hydrated oxygen (H—O-H), C—O&C-S, and $C = O$ species respectively. The S2p signal obtained from XPS analysis of the PANI@SOAM-Cy HCP nanocomposite originated from those sulfonyldianiline units deconvolutes into couple bands of S-O 2p3/2 and S-O 2p1/2 at 168.75 and 167.7 eV, respectively (Fig. 2d). Following the aniline polymerization onto the surface of SOAM-Cy HCP, XPS of the derived PANI@SOAM-Cy HCP shows similar signals of C1s to those of the SOAM-Cy HCP. The C1s peaks divided into four bands at B.Es of 287.90, 285.50, 284.82, and 284.15, corresponding to π-π*, C—N, C—O or C-S, and C═C, respectively (Fig. 2a).

From quantitative analysis point of view when focus on the C1s peaks, which typically represent various carbon states in the current materials. Firstly, considering the fitting analysis based on the FWHM and area under the peaks (Table S1) for different carbon environments, the π-π interaction peak at 287.9 eV is present in SOAM-Cy HCP and PANI@SOAM-Cy HCP but not in PANI alone. The reduction in both FWHM and area in PANI@SOAM-Cy HCP compared to SOAM-Cy HCP indicates a lower concentration and less broadening of π-π interactions when PANI is integrated with SOAM-Cy HCP. This suggests that the integration process might potentially affect the π-π stacking due to changes in the polymeric structure or interaction dynamics. The C—N peak is present in all three samples, with PANI having the largest area and widest peak. The FWHM and area decrease in PANI@SOAM-Cy HCP compared to PANI and SOAM-Cy HCP alone. This decrease suggests that the C—N bonding environment is altered when PANI is incorporated into SOAM-Cy HCP, possibly due to interaction or blending effects that reduce the overall number of C—N bonds or their homogeneity. Furthermore, the C—O and C-S peaks show a slight increase in FWHM and a significant increase in area for the PANI@SOAM-Cy HCP. This indicates an increase in these bonding environments when PANI is integrated with SOAM-Cy HCP. The higher area suggests a higher concentration of these bonds, possibly due to new interactions or bonds formed between PANI and SOAM-Cy HCP components as we earlier expected from FTIR record. The C═C peak is present in all samples, with a slight decrease in both FWHM and area in PANI@SOAM-Cy HCP compared to the individual components. This suggests that the concentration of C═C bonds is slightly reduced in the integrated material, which might be due to interactions between PANI and the SOAM-Cy HCP affecting the overall carbon structure.

Throughout focusing on the couple N1s environments identified as C═N—H and N═C. The fitting data includes the FWHM and the area under the peaks for different N1s environments. We observe that the C═N—H peak is present in all three samples but the PANI has the highest area (2965.28), indicating uplevels concentration of C═N—H

bonds in comparison to other samples, the SOAM-Cy HCP shows a lower area (2266.03) and a narrower peak (FWHM = 1.31), suggesting a lower concentration of C═N—H bonds and a more homogeneous bonding environment. Importantly, the PANI@SOAM-Cy HCP has an intermediate area (2405.08) and slightly broader peak compared to the SOAM-Cy HCP but narrower than pristine PANI, indicating that the integration of PANI with SOAM-Cy HCP affects the N═C—H bonding environment by slightly increasing the concentration compared to the SOAM-Cy HCP alone. Otherwise, the aromatic N═C peak is not present in PANI but is observed in both SOAM-Cy HCP and PANI@SOAM-Cy HCP. The SOAM-Cy HCP has a smaller area (1589.14) and narrower peak (FWHM = 1.16), indicating a lower concentration of N═C bonds and a more homogeneous bonding environment but the PANI@SOAM-Cy HCP shows a similar area (1539.84) but a much broader peak (FWHM = 3.09), suggesting a more heterogeneous bonding environment with the same concentration of N═C bonds as in SOAM-Cy HCP. The broadening of the peak indicates that integrating PANI with SOAM-Cy HCP creates a more complex nitrogen bonding environment. Here we can assume the hydrogen bonding between those N sites of the SOAM-Cy HCP and H of PANI strengthening the PANI@SOAM-Cy HCP composite.

Realistically, the S-O (2p3/2) peak is not observed in PANI as expected but is present in SOAM-Cy HCP and PANI@SOAM-Cy HCP. The SOAM-Cy HCP shows an area of 681.96 with a FWHM of 1.25, indicating a moderate concentration of S-O (2p3/2) bonds in a relatively homogeneous environment. Otherwise, the PANI@SOAM-Cy HCP shows a significantly decreasing area up to 138.34, with a slightly broader FWHM of 1.29. This suggests a much lower concentration of S-O (2p3/2) bonds in the integrated sample, indicating that the integration process significantly affects the presence of these bonds. Considering the O1s, firstly for PANI, the FWHM values for H—O-H, C—O, and C═O peaks are 1.31, 1.21, and 1.30, respectively, with corresponding peak areas of 1099.12, 1276.94, and 1496.93, indicating notable amounts of oxygen functionalities. The SOAM-Cy HCP shows FWHM values of 1.15, 0.87, and 0.86 for H—O-H, C—O, and C═O, respectively, with larger peak areas of 1527.63, 1609.43, and 1076.82, reflecting the extensive presence of oxygen-containing groups. In the PANI@SOAM-Cy HCP composite, the FWHM values for H—O-H, C—O, and C═O peaks are 1.70, 1.17, and 1.19, respectively, with peak areas of 979.43, 1081.03, and 712.04, indicating a reduction in oxygen functionalities compared to the individual components. These differences in FWHM and peak areas suggest that the integration of PANI with SOAM-Cy HCP alters the chemical environment and reduces the number of oxygen-containing groups, likely due to interactions between PANI and the SOAM-Cy HCP framework utilizing those S═O units.

Consecutively, the S-O (2p1/2) peak is also not observed in PANI but is present in the SOAM-Cy HCP and PANI@SOAM-Cy HCP. For the SOAM-Cy HCP, the area is 614.655 with a FWHM of 0.88, indicating a moderate concentration of S-O (2p1/2) bonds in a relatively homogeneous environment. For the PANI@SOAM-Cy HCP, the area decreases to 154.02 with a slightly narrower FWHM of 0.86. This suggests a significantly lower concentration of S-O (2p1/2) bonds in the integrated sample, similar to the trend observed for the S-O (2p3/2) bonds. The S2p XPS data indicates that the S-O bonding environments are significantly affected by the integration of PANI with SOAM-Cy HCP. Specifically, the concentration of S-O bonds (both 2p3/2 and 2p1/2) is much lower in the integrated sample (PANI@SOAM-Cy HCP) compared to SOAM-Cy HCP alone. This suggests that the integration process leads to a reduction in the S-O bonding, assumes due to changes in the chemical environment or interactions between PANI and the SOAM-Cy HCP components. This modification can enhance the composite's electrochemical properties by optimizing the balance between conductive pathways and active sites for ion adsorption, making the PANI@SOAM-Cy HCP composite a promising material for supercapacitor applications.

3.3. Thermogravimetric analysis

The thermal gravimetric analysis (TGA) data for the PANI, SOAM-Cy HCP, and PANI@SOAM-Cy HCP (Fig. S2) reveals significant insights into their thermal properties. The decomposition temperature at 10 % weight loss (T_{d10}) for PANI is 304.8 °C, indicating it is the least thermally stable among the three samples. On the other hand, SOAM-Cy HCP shows improved thermal stability with a T_{d10} of 325.20 °C. Remarkably, PANI@SOAM-Cy HCP demonstrates the highest thermal stability with a T_{d10} of 392.7 °C, highlighting the positive effect of integrating PANI with SOAM-Cy HCP on thermal stability. We assume the increment of thermal stabilities based the PANI@SOAM-Cy HCP due to the hydrogen bonding between the forming components as we explained within the XPS section.

In terms of char yield, which emphasizes the residual after thermal degradation, PANI exhibits a moderate char yield of 33.5 wt.%. The SOAM-Cy HCP has a slightly lower char yield at 28.0 wt.%, suggesting little resistance to thermal degradation compared to PANI. Importantly, the PANI@SOAM-Cy HCP has the highest char yield at 44.0 wt.%, indicating the best resistance to thermal degradation among the three samples. This suggests that the integration process significantly enhances the material's resistance to thermal decomposition, resulting in a higher amount of residue. Thereby, the TGA data clearly demonstrates that integrating PANI with the SOAM-Cy HCP results in a material with superior thermal stability and extreme resistance to thermal degradation, as evidenced by the highest T_{d10} and char yield in the PANI@SOAM-Cy HCP composite.

3.4. BET analyses

The surface area and porosity data of the PANI, SOAM-Cy HCP, and PANI@SOAM-Cy HCP composites provide insights into their potential performance as materials for supercapacitors (Fig. S3a). PANI exhibits the lowest surface area (22.9 m^2/g) and lacks measurable porosity, indicating limited sites for ion adsorption and charge storage. In contrast, the SOAM-Cy HCP has a significantly higher surface area (38.31 m^2/g) as well as a substantial pore volume (0.703 cm^3/g), with a range of pore widths (1.191 nm, 2.184 nm, 3.93 nm, and 8.05 nm) (Fig. S3b), showing a highly porous structure conducive to efficient ion transport and charge storage. This hierarchical porosity is advantageous for supercapacitor applications, as it facilitates rapid ion diffusion and increases the electrode-electrolyte junction area, thereby improving the capacitance as well as charge-discharge rates.

Upon integrating PANI with SOAM-Cy HCP, the resulting PANI@SOAM-Cy HCP nanocomposite shows an intermediate surface area (23.6 m^2/g) and a drastically reduced pore volume (0.035 cm^3/g). The pore widths (1.27 nm, 2.25 nm, 7.14 nm, and 9.34 nm) remain diverse, indicating that some porosity of the former SOAM-Cy HCP is still retained, and the overall pore volume is significantly decreased. This result suggests that PANI incorporation leads to the filling or blocking of some pores, reducing the effective porosity. However, the retained hierarchical pore structure in PANI@SOAM-Cy HCP could still facilitate ion diffusion, albeit to a lesser extent than SOAM-Cy HCP alone. Otherwise, the higher surface area and improved porosity compared to the pure PANI enhance the PANI@SOAM-Cy HCP ability for charge storage through electrical double-layer capacitance and pseudocapacitance mechanisms. Realistically, in supercapacitors, these structural properties are crucial. The SOAM-Cy HCP's wide surface area as well as pore volume provides numerous active positions for ion adsorption and storage, leading to higher capacitance and faster charge-discharge cycles. In spite of the lower pore volume the PANI@SOAM-Cy HCP, it can combine benefits from the blend of electrical conductivity from PANI as well the hierarchical porous frame of the SOAM-Cy HCP, potentially resulting in enhanced supercapacitive performance compared to PANI alone. This composite material could thus offer a balance between structural integrity, ion accessibility, and electrical

conductivity, making it a promising candidate for high-performance supercapacitors.

3.5. Morphology measurements

The TEM images reveal the morphological characteristics for PANI, SOAM-Cy HCP, and PANI@SOAM-Cy HCP. PANI (Fig. 3a-b) shows an irregular, aggregated structure with dense regions, indicating a non-porous material, consistent with its low surface area and little pore volume. In contrast, the SOAM-Cy HCP (Fig. 3c-d) displays a highly porous network with varying pore sizes owing to its wide surface area and fundamental pore volumes. The interconnected, and lighter regions throughout the visions suggest efficient pathways for ion transport thereby considers beneficial units for supercapacitor electrodes. The PANI@SOAM-Cy HCP nanocomposite (Fig. 3e-f) combines features of both materials, showing areas of dense PANI and porous SOAM-Cy HCP. Although the PANI@SOAM-Cy HCP nanocomposite retains some porosity, the limited pore volume indicates partial pore filling or blockage by the coated PANI. Importantly, this mixed morphology of the PANI@SOAM-Cy HCP implies that the integration of PANI reduces overall porosity, thereby enhances conductivity, providing a balance that can improve supercapacitor performance by combining the conductive properties of PANI with the porous structure of SOAM-Cy HCP.

The morphological characteristics of pure PANI, SOAM-Cy HCP, and the PANI@SOAM-Cy HCP nanocomposite were deeply examined utilizing scanning electron microscopy (SEM). Fig. 3g exhibits the SEM image of the bare PANI, revealing predominantly jungle-like spherical structures. In contrast, Fig. 3h illustrates the morphology of pristine SOAM-Cy HCP, where distinct spherical particles are observed, not interconnected. Fig. 3i displays the morphology of the PANI@SOAM-Cy HCP nanocomposite, showing a uniform coating of PANI onto the inner and outer layers of SOAM-Cy HCP. These observations suggest that the surface of SOAM-Cy HCP provides ample nucleation sites, which are advantageous for the continuous growth of the PANI layer, allowing ions to penetrate deeply into the electrode surface.

The atomic maps of the PANI, SOAM-Cy HCP, and PANI@SOAM-Cy HCP nanocomposite attribute the dispersion of C, N, O, and S elements onto their surfaces (Fig.S4a-c). Moreover, the Energy-dispersive X-ray spectroscopy (EDX) shows the elemental makeup of the PANI, SOAM-Cy HCP, and PANI@SOAM-Cy HCP nanocomposite (Fig. S5) confirming those earlier results of the elemental mapping and XPS scans.

3.6. Electrochemical performance

The CV curves for the PANI, SOAM-Cy HCP, and PANI@SOAM-Cy HCP, estimated in the three electrode configuration using a 0.5 M H$_2$SO$_4$ electrolyte, providing a crucial insight into the electrochemical efficacy of these moieties. The CV tracks were recorded at different scan rates spanning between 5 and 200 mV s^{-1} within the potential range of −0.3 to 0.5 V, as depicted in Fig. 4a-c respectively. A quasi-rectangular shape with some distortion is visible in the CV tracks of the PANI at higher scan rates (Fig. 4a). It demonstrates the standard action of electric double-layer capacitance (EDLC) incorporating contributions from pseudocapacitance. Redox peaks indicate the presence of faradaic reactions, which are typical of PANI because of its conductive nature. The current response shows strong capacitive behaviour as the scan rate increases, albeit with certain restrictions in the charge transfer kinetics at uplevels scan rates. On the other hand, the CV tracks for SOAM-Cy HCP (Fig. 4b) exhibit a more ideal rectangular shape, indicating a predominant EDLC behavior with minimal pseudocapacitive contributions. This is consistent with the large surface area and porous frames observed in the TEM and BET analyses, facilitating efficient ion adsorption and desorption. Moreover, this limited faradic capacitance of the SOAM-Cy HCP originates from the redox of the triazine ring as described et al. [55]. The current response scales linearly with increasing scan rates,
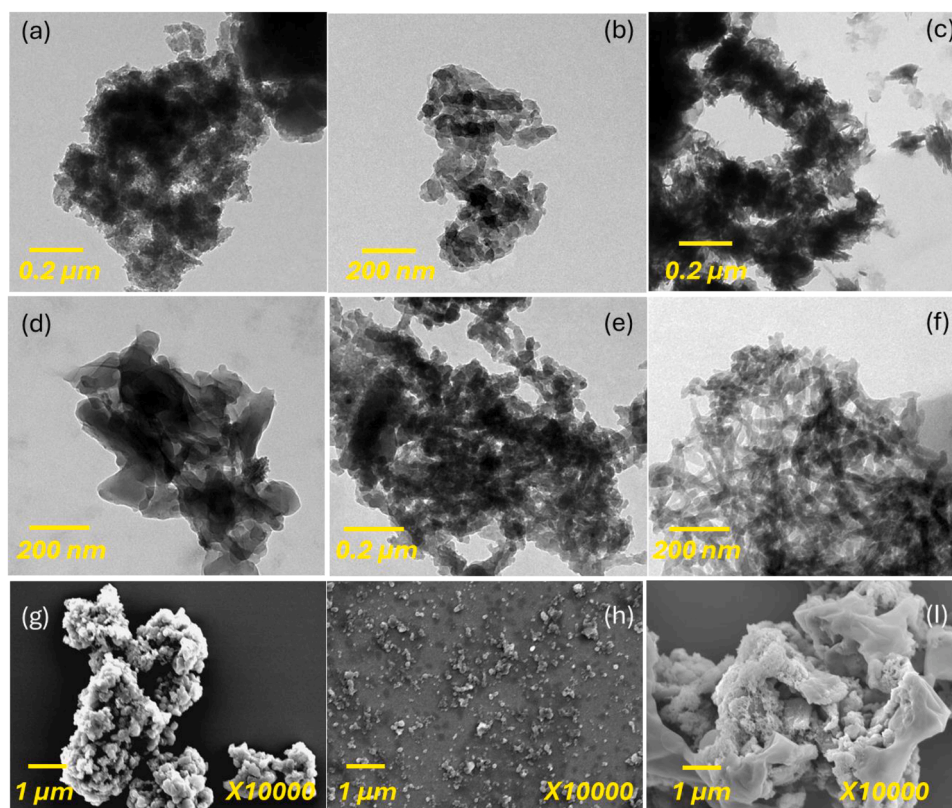
Fig. 3. TEM scanning at different magnifications (a-f) and SEM visualizations (g-i) of the PANI (TEM: a-b, SEM: g), SOAM-Cy HCP (TEM: c-d, SEM: h), and PANI@SOAM-Cy HCP nanocomposite (TEM: e-f, SEM: i).

implies excellent rate capability and fast ion mobility throughout the porous structure of the SOAM-Cy HCP. The minimal disfigurement at higher scan rates emphasizes the robust electrochemical robustness and exceptional reversibility within the charge-discharge turns [56,57].

Importantly, the CV curves for the PANI@SOAM-Cy HCP nanocomposite (Fig. 4c) emphasizes an integration of those features observed in both PANI and SOAM-Cy HCP. The CV curves (Fig. 4c) show quasi-rectangular tracks have noticeable redox humps, indicative of both EDLC and pseudocapacitive processes. Notably, such incorporation of PANI into the SOAM-Cy HCP matrix enhances the faradaic reaction sites, contributing to the pseudocapacitance while maintaining good EDLC properties due to the retained porosity [4,58]. Obviously, the current output clearly improves with scan rate, indicating superior rate capability and electrochemical functionality in contrast with the standard PANI. The combination of SOAM-Cy HCP's high surface area and porosity with PANI's conductive pathways delivers a synergistic outcome that makes the composite an interesting electrode material for outstanding-performance supercapacitors. Overall, the CV statistics show that PANI contributes significantly to pseudocapacitive behavior, while SOAM-Cy HCP gives good EDLC behavior because of its large surface area as well as porosity. Therefore, the PANI@SOAM-Cy HCP composite combines the advantages of each component to provide augmented electrochemical activity by combining pseudocapacitance with EDLC, which makes it a desirable option for supercapacitor devices. Thereby, such ability of the PANI@SOAM-Cy HCP composite to maintain a high current response across a range of scan rates underscores its potential for dynamic-rate and improved-capacity energy storage.

The GCD analysis reveals significant and deeper insights into the electrochemical behavior of the proposed materials (Fig. 4 d-f). Firstly, the triangular-shaped GCD curves of PANI (Fig. 4d) and PANI@SOAM-Cy HCP (Fig. 4f), with slight bending, demonstrate the prospect toward significant capacitance utilizing the integration of the fundamental concepts of EDLC and pseudocapacitance. Otherwise, the SOAM-Cy

HCP's more linear GCD tracks imply a major contribution of EDLC characteristic than pseudocapacitance. Furthermore, the longer discharging times of PANI and PANI@SOAM-Cy HCP compared to the SOAM-Cy HCP suggest higher specific capacitances of formers. The PANI, SOAM-Cy HCP, and PANI@SOAM-Cy HCP record specific capacitances of 249.22 F g^{-1}, 39.48 F g^{-1}, and 678.93 F g^{-1}, respectively at a current density of 1 A g^{-1} (Fig. 5a), these finding arising those reported porous organic materials as shown in the comparison study of Table S2. These findings align with the CV statics, demonstrating the higher electrochemical efficacy of the PANI@SOAM-Cy HCP composite, which reveals the synergistic conductivity of PANI alongside the large surface area as well as the porous frame of the SOAM-Cy HCP. Ultimately, the GCD conductions impart the suitability of the PANI@SOAM-Cy HCP composite for facilitating the rate and capacity within supercapacitor.

From the porosity point of view of PANI, SOAM-Cy HCP, and PANI@SOAM-Cy HCP we can provide valuable insights into their potential as supercapacitor materials. PANI's low surface area and lack of measurable porosity suggest minimized ion adsorption sites, therefore primarily relying on surface adsorption for capacitance as a conducting polymer. Again, in the case of PANI, its low surface area and lack of measurable porosity indicate that it has limited active sites for ion adsorption and restricted pathways for ion diffusion. As a result, PANI suffers limited overall performance in contrast to materials with higher surface area and porosity. Otherwise, the SOAM-Cy HCP has a large surface area, substantial pore volume, as well as diverse pore widths consequently demonstrates a highly porous framework conducive to efficient ion transport and charge storage, leading to higher capacitance and dynamic charge-discharge rates. Despite a reduction in pore volume upon PANI incorporation, PANI@SOAM-Cy HCP retains a hierarchical pore framework that could enhance ion diffusion and offers improved capacitance compared to PANI alone. This composite's balance between structural integrity, ion accessibility, and electrical conductivity making
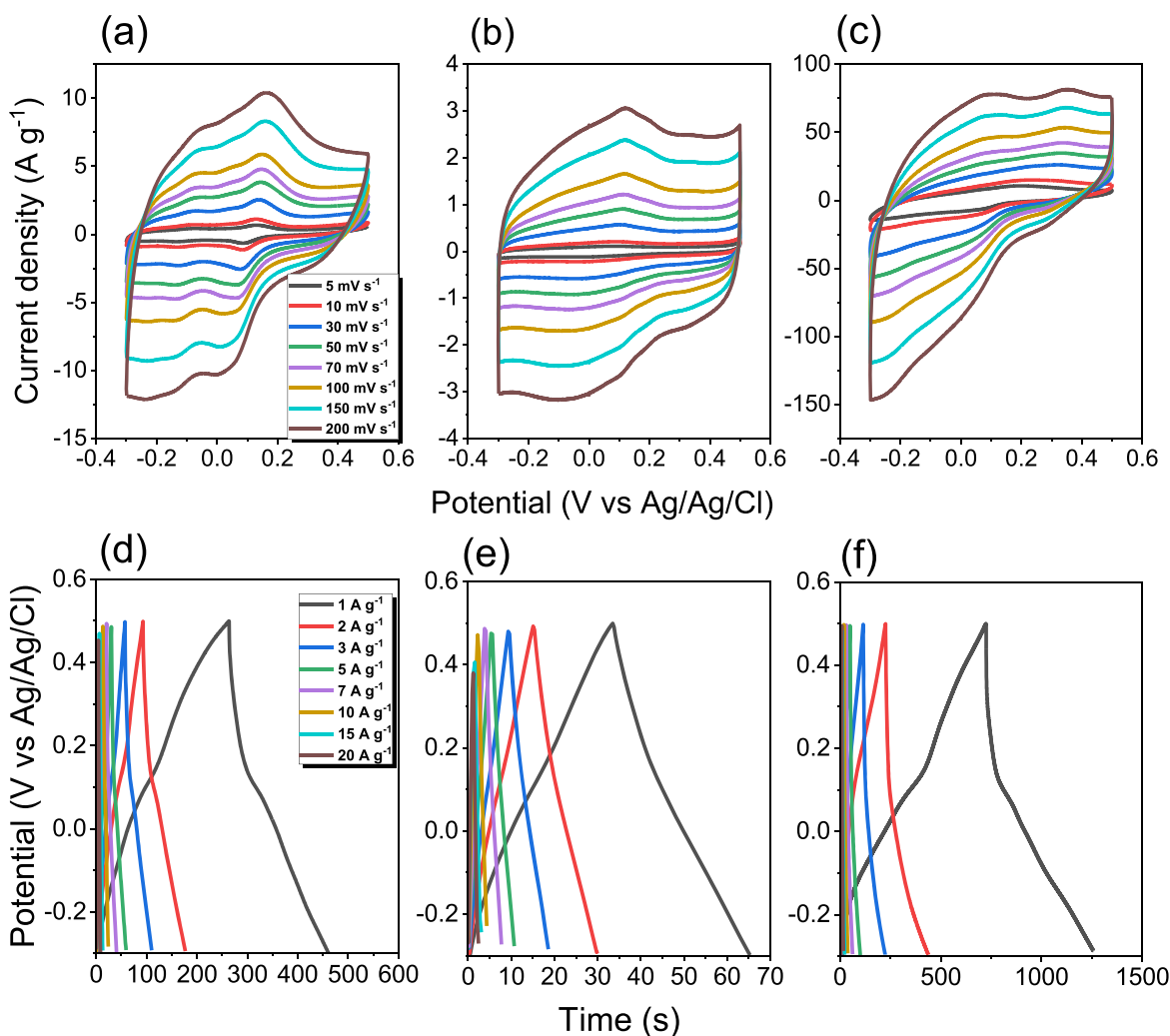
Fig. 4. Cyclic voltammetry sweeps of those PANI (a), SOAM-Cy HCP (b), and PANI@SOAM-Cy HCP composite(c) in the potential range of −0.3–0.5 V under many sweep rates, GCD sweeps of those PANI (d), SOAM-Cy HCP (e), and PANI@SOAM-Cy HCP composite(f) at various current densities.

it as an attractive option for high-performance supercapacitors owing to the strengths of both PANI and SOAM-Cy HCP.

Ragone plots serving as essential tools for assessing the performance of energy storage materials, especially in supercapacitors, throughout illustrating the trade-off between energy density and power density. Throughout the current research, PANI and PANI@SOAM-Cy HCP display significant power densities than the SOAM-Cy HCP, as shown by Ragone plots (Fig. 5b) based on the given equations and a voltage window in-between −0.3 and 0.5 V. This shows that PANI and PANI@SOAM-Cy HCP nanocomposite have superior capabilities for rapid energy delivery. Under a current density of 500 W kg^{-1}, the energy densities of PANI, SOAM-Cy HCP, and PANI@SOAM-Cy HCP are 34.61, 5.48, and 94.29 W h kg^{-1}, respectively (Fig. 5b). Notably, such energy density of PANI@SOAM-Cy HCP nanocomposite surpasses those of PANI and SOAM-Cy HCP, suggesting that the former nanocomposite can store more energy per unit mass. Furthermore, the Ragone figures suggest that the power densities of cells depend on PANI and PANI@SOAM-Cy HCP can exceed those of other reported supercapacitors as displayed by Table S3, demonstrating the fruitful potential of this nanocomposite toward high-performance energy storage applications where both power delivery and energy storage capacity are crucial. Long-term capability of supercapacitors depends on the stability of their incorporated electrode polymers [59]. Unfortunately, it is commonly known that conducting

polymers, like PANI, expand and swell upon charge/discharge turns [14]. This can cause mechanical stress and eventual breakdown, decreasing the stability of this family. Otherwise, HCPs can minimize these defects hence offer higher stability over charge/discharge turns. The SOAM-Cy HCP and PANI@SOAM-Cy HCP demonstrate exceptional durability even after 5000 turns under a current density of 10 A g^{-1}, they record retention Coulomb efficiencies to 93.9 % and 86.0 %, respectively (Fig. 6).

This indicates that these materials can maintain a high level of charge-discharge efficiency over multiple cycles, suggesting good stability. On the other hand, as we expected above the PANI shows a lower retention Coulomb efficiency of around 23.89 % after 5000 turns, indicating a higher degree of degradation and lower stability compared to the SOAM-Cy HCP or PANI@SOAM-Cy HCP (Fig. 6b). Despite the differences in stability degrees, PANI, SOAM-Cy HCP, and PANI@SOAM-Cy HCP show specific capacitances of 32.26, 25.04, and 203.49 F g^{-1} after 5000 turns at a current density of 10 A g^{-1} (Fig. 6a). The improved stability of the SOAM-Cy HCP and PANI@SOAM-Cy HCP compared to PANI can be attributed to the incorporation of the PANI into the porous SOAM-Cy HCP matrix, which may help to mitigate the mechanical stress and degradation typically associated with PANI. Furthermore, the hierarchical porosity of SOAM-Cy HCP provides structural support and accommodates the volume changes of PANI
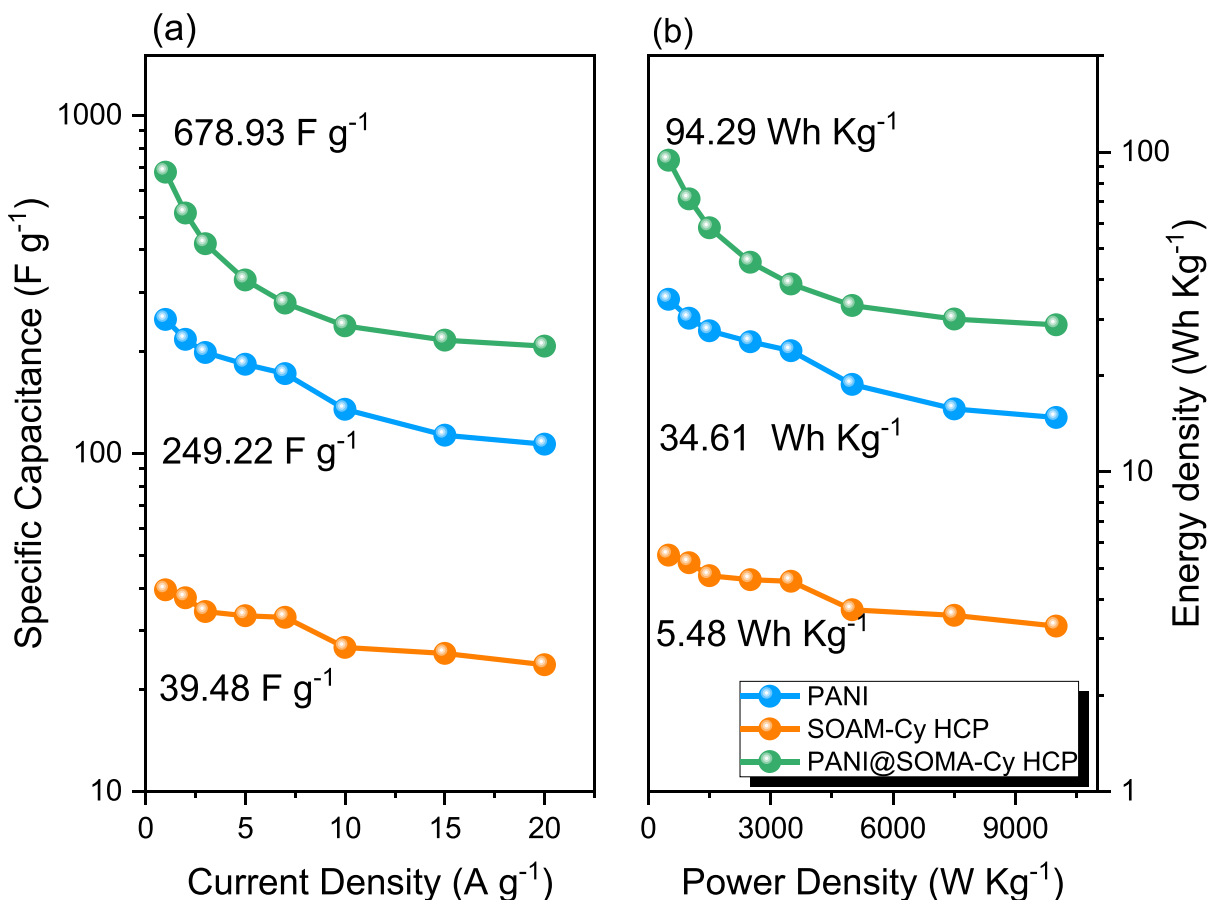
Fig. 5. (a) Specific capacitance of the PANI, SOAM-Cy HCP, and PANI@SOAM-Cy HCP composite at numerous current densities in between 1 and 20 A g^{-1} and (b) Ragone plots of them.

during cycling, leading to enhanced stability and better performance over long term cycling. The EIS outcomes provide valuable insights into the ion transport behavior and internal ohmic resistance of those PANI, SOAM-Cy HCP, and PANI@SOAM-Cy HCP. The faint arcs seen at high frequencies in the EIS studies refer to mass transport and resistive charge transfer (R_{CT}) actions taking place in the materials we use. The equivalent series resistance (ESR), which consists of electrolyte resistance, intrinsic resistance found in the electrode matrix, and interface resistance across the electrode with current collector, is illustrated by junctions of these arcs with the x-axis. The enormous surface areas of the nanocomposite and synthetic HCP provide a large area of contact for interaction with SO_4^{2-} ions, indicating the possibility of more active regions for energy storage. This is mirrored in the lower ESR assessments, which show superior conductivity and larger capacity for energy storage. Additionally, heteroatoms on the electrode surfaces improve wettability, which amplifies the electrochemical efficiency significantly. The Nyquist curves confirm these findings, with PANI, SOAM-Cy HCP, and PANI@SOAM-Cy HCP displaying resistance values of 8.35 Ω, 21.81 Ω, and 5.11 Ω, respectively (Fig. S6a) and fitted within the electrical circuit of Fig. S6b. Superior specific capacitance and improved energy storage capacity for the electrode content are demonstrated by these minimized resistance levels. The Bode plots (Fig. S6c) validate the materials' favorable electrical properties by giving diagonal aligned with a downward slope under lower frequencies alongside depressed ohmic resistance levels under higher frequencies. The frequency-dependent phase-angle of Bode plots (Fig. S6d) determine knee frequencies of

139.19 Hz for PANI, 847.8 Hz for SOAM-Cy HCP, and 679.9 Hz for PANI@SOAM-Cy HCP respectively thereby demonstrating outstanding electrochemical efficiencies, under higher knee frequencies displaying their better rate performance. Overall, these findings emphasize the prospective applications of the designed PANI@SOAM-Cy HCP nanocomposite in high-performance supercapacitors by showing that they have low ESR, high specific capacitance, and superb rate effectiveness.

Exclusively, the PANI@SOAM-Cy HCP exhibits promising characteristics for supercapacitor applications. With an ESR of 5.11 Ω, lower than those of the SOAM-Cy HCP and PANI, it demonstrates improved conductivity and efficient charge transfer, leading to higher specific capacitance. The material's significant surface area provides ample contact points for interaction with SO_4^{2-} ions, indicating additional active sites for energy storage as we explained above throughout CV and GCD analysis. This feature, coupled with a knee frequency of 679.9 Hz, suggests excellent rate efficiency, enabling high performance even at rapid charge-discharge rates. As an appropriate choice for high-performance supercapacitors, PANI@SOAM-Cy HCP delivers reasonable balance of energy storage capacity along with power transmission overall.

The superior rate capability of PANI@SOAM-Cy HCP is evidenced by a significant capacitive contribution to its total capacity. This contribution was quantified using the relation where the total current i(V) at a constant potential V is the sum of the currents from diffusion-controlled ($k_2v^{1/2}$) and capacitive (k_1v) mechanisms (Fig. 7a) where values of k_1 and k_2 were detected depending on the slope as well as the intercept of
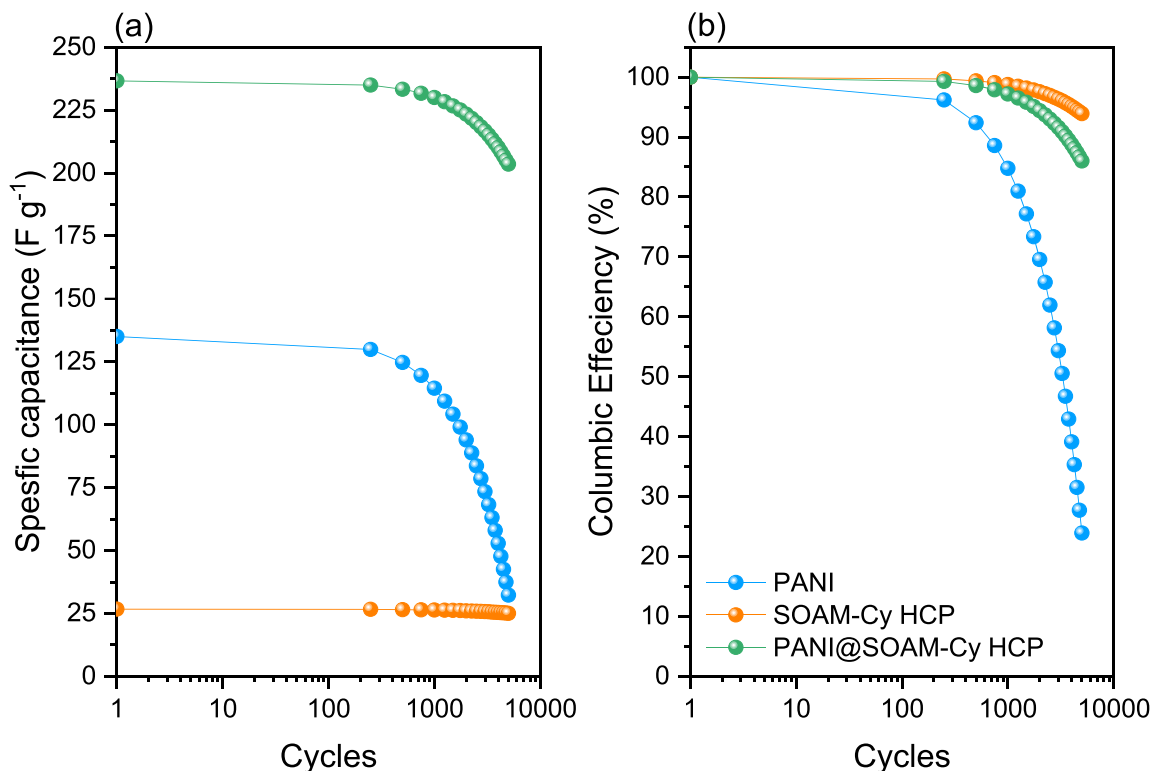
Fig. 6. (a) Specific capacitances and (b) columbic efficiency of the PANI, SOAM-Cy HCP, and PANI@SOAM-Cy HCP composite within various 5000 cycles at 10 A g^{-1}.

eq. (1)–2. At a low scan rate of 5 mV s^{-1}, the capacitive contribution was 75.48 %, while the diffusion-controlled contribution was 24.52 % of the total capacity (Fig. 7b-c). As the scan rate increased from 5 to 200 mV s^{-1}, the capacitive contribution decreased to 54.86 % (Fig. 7b). This reduction in capacitive contribution under quick scan emphasize that while PANI@SOAM-Cy HCP maintains a significant capacitive behavior, the role of diffusion-controlled processes becomes more pronounced at faster scan rates. A power law (Eq. 7) was utilized to examine the relation in-between electrical current (i) with scan rates potential (v) in order to investigate the capacitive impact of PANI@SOAM-Cy HCP. The slope of a log(i) versus log(v) plot was utilized to estimate the value of "b" (Fig. 7d), which helps differentiate between capacitive and diffusion-controlled mechanisms. For PANI@SOAM-Cy HCP, the calculated b numbers were 0.5299 and 0.522 for the anodic and cathodic peaks respectively. Those b values, which are in the neighborhood of 0.5, point to a combination of bulk diffusion-controlled along with capacitive (surface-controlled) energy storage systems. Ultimately, these results demonstrate that PANI@SOAM-Cy HCP has a significant capacitive impact which is helpful in rapid charge-discharge turns, particularly at lower scan rates. However, the diffusion- controlled mechanisms also become more significant as the scan rate rises, demonstrating the material's capacity for both rapid and long-term energy storage.

$$i(v) = k_1 v + k_2 v^{1/2} \qquad (1)$$

$$\frac{i(v)}{v^{1/2}} = k_1 v^{1/2} + k_2 \qquad (2)$$

$$i = a v^b \qquad (3)$$

3.7. Coin cell device

The study of PANI@SOAM-Cy HCP in a two-electrode symmetric coin supercapacitor provides important new understandings concerning its future prospects for real-world use. The PANI@SOAM-Cy HCP-based symmetrical coin cell's CV sketches were recorded at different sweep scans in-between 5 and 200 mV s^{-1} over a potential ranges of 0.5 to 0 V. The CV tracks had a characteristic rectangular curve even at high sweep speeds (200 mV s^{-1}) as observed in Fig. 8a. This emphasize that the capacitance was an EDLC type. This implies that PANI@SOAM-Cy HCP can continue to function at high scan rates by quickly and effectively storing and releasing charges. The excellent reversibility of the symmetric capacitor, which is essential for the durability and dependability of supercapacitors, is further shown by a rise in current at higher scan rates. The PANI@SOAM-Cy HCP-based symmetric cell's GCD profiles (Fig. 8b) show a triangular shape, which suggested strong capacitance efficiency along with dynamic energy storage power. The GCD curves' triangular shape suggests steady charge-discharge turns with impalpable resistive distortions, demonstrating the capacitor's effectiveness. The electrochemical capacitance of the PANI@SOAM-Cy HCP was 325.00 F g^{-1} at a current density of 1.0 A g^{-1} (Fig. 8c). This reading demonstrates the high performance of the PANI@SOAM-Cy HCP nanocomposite across all trial settings, as it exceeds the capacitance for numerous earlier discovered materials as well as agrees well with the results of the three-electrode trial. Realistically, the specific capacitance attitudes achieved in the two-electrode and three-electrode systems are not the same. Generally, the three-electrode setup has a specific capacitance three times extra compared to the two-electrode setup. This difference stems from the reality of the three-electrode system employs just one double layer of capacitance, while the two-electrode system uses double-layer capacitance at both electrodes, essentially acting as dual capacitors in series. Thus, the specific capacitance determined in the three-
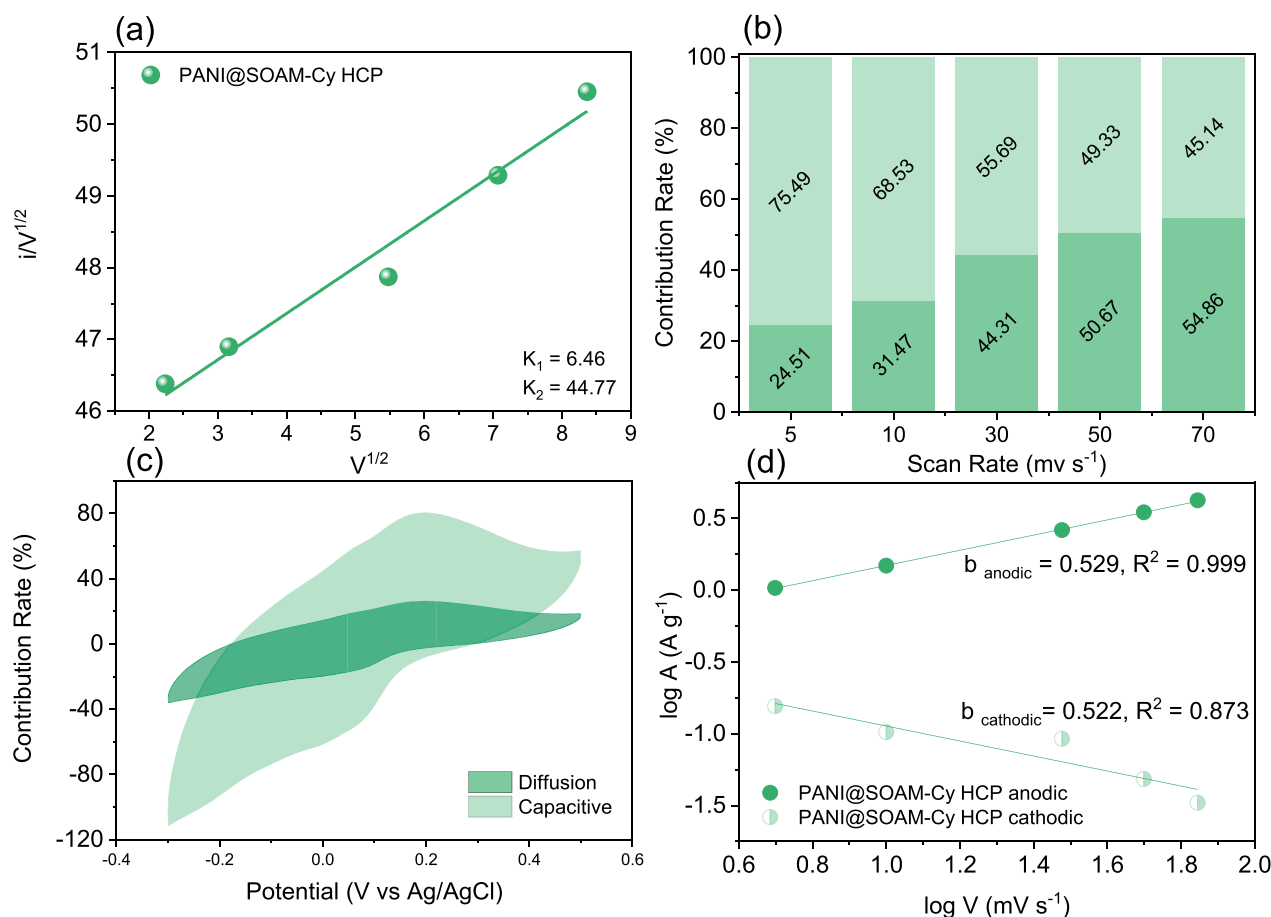
Fig. 7. (a) Plots of $v^{1/2}$ versus $i/v^{1/2}$, (b) the capacitive and diffusion integrations detected at 5 mV s^{-1}, (c) the capacitive and diffusion percentage imparted at sweep rates, (d) plots of log v versus log A at various cathodic and anodic currents (d) of the PANI@SOAM-Cy HCP.

electrode configuration claims as the substrate capacitance (C$_{material}$), whereas the particular capacitance recorded in the coin cell (two-electrode system) terms as the device capacitance (C$_{device}$).

These outcomes highlight PANI@SOAM-Cy HCP's feasibility for utilization in functional supercapacitor units. The symmetric coin cell sustains high capacitance and dynamic charge-discharge behavior indicating that this material can be employed in commercial energy storage devices. The optimum rate ability, high reversibility, and outstanding specific capacitance all highlight the potential of PANI@SOAM-Cy HCP as a high-performance supercapacitor material. Moreover, this study confirms that PANI@SOAM-Cy HCP not only performs well in laboratory-based three-electrode systems but also translates this performance into commercially relevant two-electrode systems, positioning it as a fruitful candidate for advanced supercapacitors.

As we mentioned above, the Ragone plot is a crucial tool in evaluating the performance of energy storage devices, as it provides a visual representation of the correlation in-between energy density and power density. For the PANI@SOAM-Cy HCP based symmetric cell, the Ragone plot illustrates a remarkable balance between these two key parameters. Specifically, the PANI@SOAM-Cy HCP electrode demonstrated an impressive energy density of 45.14 W h kg^{-1} at a power density of 500 W kg^{-1} (Fig. 8d). This high energy density indicates that the material can store a significant amount of energy, positioning it convenient for instruments requiring sustained energy output over longer periods. Moreover, the PANI@SOAM-Cy HCP electrode preserve a substantial energy density of 17.73 W h kg^{-1} even at a much higher power density of 10,000 W kg^{-1} (Fig. 8d). The power density of the PANI@SOAM-Cy

HCP electrode device exceeded those polymeric based electrodes reported previously (Table S4). This performance is especially remarkable because energy density normally drops as power density increases because of the constraints within the rate whereby functions like charge and discharge may occur. However, the PANI@SOAM-Cy HCP's ability to retain a relatively high energy density at elevated power densities suggests excellent rate capability and efficient charge-transfer kinetics.

This enhanced efficiency demonstrates the efficient synergy between SOAM-Cy HCP and PANI, which combines the extensive surface area and systematic porosity of SOAM-Cy HCP alongside the significant conductivity and pseudocapacitive nature of PANI. High power and energy densities are probably caused by the hierarchical porous structure, which also lowers internal resistance and speeds up ion mobility. The PANI@SOAM-Cy HCP is an intriguing nanocomposite for enhanced supercapacitors due to its increased energy density at both intermediate and uplevels-power densities when compared to previously reported materials. Such material can effectively bridge the gap between batteries and traditional capacitors, offering both high energy storage and rapid power kinetics, making it ideal for a wide range of uses between portable electronics to electric vehicles. The electrochemical impedance spectroscopy (EIS) data for the PANI@SOAM-Cy HCP electrode material (Fig. S7a) provides critical insights into its resistance characteristics and ion transport behavior within a coin cell configuration. The Nyquist plot (Fig. S7a) shows distinct semicircular features at high-frequency values for all samples, which are indicative of the R_{ct} within the electrode and fitted to the circuit of Fig. S7b. Notably, the PANI@SOAM-Cy HCP electrode exhibits the minimized R_{ct} value of 3.8 Ω, implying the efficient electron charge mobility. Further, this low R_{ct} imparts that the
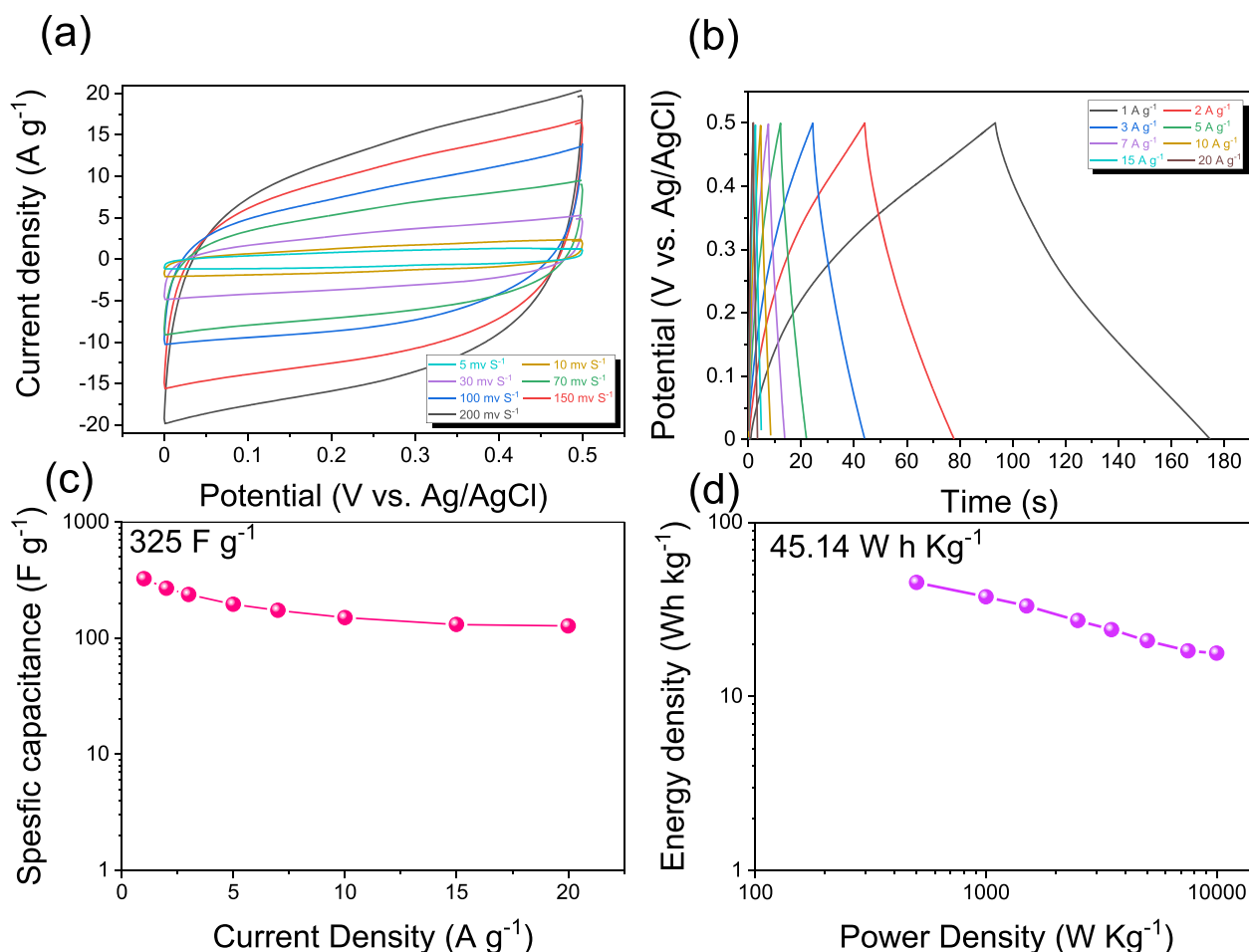
Fig. 8. (a) Cyclic voltammetry sweeps of the PANI@SOAM-Cy HCP nanocomposite in the potential window of 0–0.5 V under various sweep rates-based coin device, (b) the GCD sweeps of the PANI@SOAM-Cy HCP nanocomposite at various current densities-based coin device, (c) detected GCD specific capacitance of the PANI@SOAM-Cy HCP, and (d) Ragone plot of the PANI@SOAM-Cy HCP based the coin cell device.

PANI@SOAM-Cy HCP coated electrode has diminished internal resistance, hence facilitates rapid charge/discharge turns, consequently enhancing the ultimate performance of the incorporated supercapacitor.

Additionally, the Bode plots (Fig. S7c) provide further details about the resistance features and dynamic behavior of the PANI@SOAM-Cy HCP electrode. The negative slopes at lower frequencies in the Bode plots signify good capacitive behavior and efficient ion mobility within the electrode material. At higher frequencies, the minimal ohmic resistance observed suggests that the electrode material maintains low resistive losses during high-rate charge and discharge processes. This feature is prospect for those devices requiring rapid energy transmission. The calculated knee frequency at a 45° phase angle for the PANI@SOAM-Cy HCP (Fig. S7d) electrode is 3.42 Hz. The knee frequency emphasizes the conversion point where the capacitive behavior of the material starts to dominate over the resistive behavior. A higher knee frequency generally proves improved rate capability as well as faster ion transport within the electrode material. Therefore, the PANI@SOAM-Cy HCP shows a relatively high knee frequency which implies that it can efficiently manage high-power requirements while sustaining improved energy storage capacity [60]. The minimal charge transfer resistance, superb rate potential, and potent ion transport of the PANI@SOAM-Cy HCP electrode material have been verified by these EIS and Bode plot assessments. Since it can offer high energy and power densities with less resistive loss and to continue performing well under a variety of use circumstances, these qualities serve as a prime prospect for high-performance supercapacitors [61].

The remarkable durability and effectiveness of the PANI@SOAM-Cy HCP nanocomposites coated electrode in real-world supercapacitor applications is demonstrated by the operation of the coin cell unit that utilizes it. After 5000 charge-discharge turns at a current density of 10 A g^{-1}, the specific capacitance of the PANI@SOAM-Cy HCP electrode remains at 123.24 F g^{-1} (Fig. S8a). The nanocomposite's strong stability and capacity to tolerate continuous cycling without sustaining noticeable depreciation are demonstrated by the capacitance's retention across a considerable number of turns. It implies that the PANI@SOAM-Cy HCP nanocomposite coated electrode structure remains intact, sustaining its electrochemical activity over long term use.

The coulombic efficiency of the coin cell system, which measures the efficiency of charge transfer during cycling, is around 81.89 % (Fig. S8b). An efficiency of 81.89 % implies that a substantial portion of the charge is effectively utilized, with minimal losses during the charge-discharge turns. This high efficiency indicates good reversibility of the electrochemical reactions within the PANI@SOAM-Cy HCP nanocomposite coated electrode and efficient ion mobility mechanisms.

4. Conclusions

In this research, we have successfully created a novel composite material, PANI@SOAM-Cy HCP, by integrating PANI with HCP incorporating SOAM and Cy blocks. We have fully characterized-chemically and physically- innovated polymers and composite using advanced techniques. This innovative material combines the advantageous

properties of both PANI and HCP, resulting in improved electrochemical performance suitable for high-efficiency supercapacitor applications. The PANI@SOAM-Cy HCP composite showed a remarkable specific capacitance of 325.00 F g^{-1} at 1.0 A g^{-1}, demonstrating its potential for high-capacity energy storage. Additionally, it achieved an impressive energy density of 45.14 W h kg^{-1} at a power density of 500 W kg^{-1}, maintaining a high energy density of 17.73 W h kg^{-1} even at 10,000 W kg^{-1}. The composite also displayed outstanding cycling stability, retaining 81.89 % of its initial capacitance after 5000 cycles at 10 A g^{-1}. The enhanced performance of the PANI@SOAM-Cy HCP nanocomposite can be revealed to its high surface area, hierarchical porosity, and reduced R_{ct} of 3.8 Ω. The incorporation of SOAM and Cy further improved structural stability and provided additional active sites for ion adsorption, as confirmed by Nyquist and Bode plots. Ultimately, the PANI@SOAM-Cy HCP composite material demonstrates significant promise for next-generation supercapacitors, offering a balanced combination of high energy density, excellent cycling stability, and efficient ion transport. This work highlights the potential of integrating conductive polymers with hyper-crosslinked porous polymers to develop advanced energy storage materials with superior electrochemical properties. Future research will focus on further optimizing the nanocomposite structure and exploring its applications in various energy storage systems.

CRediT authorship contribution statement

Mohammed G. Kotp: Writing – original draft, Formal analysis, Data curation, Conceptualization. **Shiao-Wei Kuo:** Writing – review & editing, Supervision, Resources, Funding acquisition.

Declaration of competing interest

The authors declare that they have no known competing financial interests or personal relationships that could have appeared to influence the work reported in this paper.

Supplementary materials

Supplementary material associated with this article can be found, in the online version, at doi:10.1016/j.electacta.2025.146440.

Data availability

The data that has been used is confidential.

References

[1] J. Dai, J. Selvaraj, M. Hasanuzzaman, H.H. Cai, Scientometric analysis of research hotspots in electrochemical energy storage technology, J. Energy Storage 93 (2024) 112300.

[2] Z. Yan, S. Luo, Q. Li, Z.S. Wu, S. Liu, Recent advances in flexible wearable supercapacitors: properties, fabrication, and applications, Adv. Sci. 11 (2024) 2302172.

[3] Y. Gao, C. Xie, Z. Zheng, Textile composite electrodes for flexible batteries and supercapacitors: opportunities and challenges, Adv. Energy Mater. 11 (2021) 2002838.

[4] M.G. Kotp, J. Lüder, S.-W. Kuo, A.F.M. EL-Mahdy, Phenazine-integrated conjugated microporous polymers for modulating the mechanics of supercapacitor electrodes, Mater. Adv. 5 (2024) 4142–4150.

[5] M.G. Kotp, S.U. Sharma, J.-T. Lee, A.F.M. EL-Mahdy, S.-W. Kuo, Triphenylamine-based conjugated microporous polymers as dye adsorbents and supercapacitors, J. Taiwan. Inst. Chem. Eng. 134 (2022) 104310, https://doi.org/10.1016/j.jtice.2022.104310.

[6] M.A. Azam, N.S.N. Ramli, N.A.N.M. Nor, T.I.T. Nawi, Recent advances in biomass-derived carbon, mesoporous materials, and transition metal nitrides as new electrode materials for supercapacitor: a short review, Int. J. Energy Res. 45 (2021) 8335–8346.

[7] S.A. Kadam, K.P. Kadam, N.R. Pradhan, Advancements in 2D MXene-based supercapacitor electrodes: synthesis, mechanisms, electronic structure engineering, flexible wearable energy storage for real-world applications, and future prospects, J. Mater. Chem. A 12 (2024) 17992–18046.

[8] Y.A. Kumar, G.R. Reddy, T. Ramachandran, D.K. Kulurumotlakatla, H.S. Abd-Rabboh, A.A.A. Hafez, S.S. Rao, S.W. Joo, Supercharging the future: MOF-2D MXenes supercapacitors for sustainable energy storage, J. Energy Storage 80 (2024) 110303.

[9] A.F.M. El-Mahdy, C.-H. Kuo, A. Alshehri, C. Young, Y. Yamauchi, J. Kim, S.-W. Kuo, Strategic design of triphenylamine and triphenyltriazine-based two-dimensional covalent organic frameworks for CO 2 uptake and energy storage, J. Mater. Chem. A 6 (2018) 19532–19541, https://doi.org/10.1039/C8TA04781B.

[10] Z. Zhao, K. Xia, Y. Hou, Q. Zhang, Z. Ye, J. Lu, Designing flexible, smart and self-sustainable supercapacitors for portable/wearable electronics: from conductive polymers, Chem. Soc. Rev. 50 (2021) 12702–12743.

[11] M.G. Sumdani, M.R. Islam, A.N.A. Yahaya, S.I. Safie, Recent advancements in synthesis, properties, and applications of conductive polymers for electrochemical energy storage devices: a review, Polym. Eng. Sci. 62 (2022) 269–303.

[12] S.K.Verma Sonika, S. Samanta, A.K. Srivastava, S. Biswas, R.M. Alsharabi, S. Rajput, Conducting polymer nanocomposite for energy storage and energy harvesting systems, Adv. Mater. Sci. Eng. 2022 (2022) 2266899.

[13] S.M. Alsufyani, R. Jafer, J. Iqbal, R. Alwafi, S. Bashir, S. Ramesh, K. Ramesh, Carbon and polymer-based conducting platforms incorporated with electroactive metal-oxides/sulphides for energy storage devices, J. Energy Storage 84 (2024) 110713.

[14] P. Liu, J. Yan, Z. Guang, Y. Huang, X. Li, W. Huang, Recent advancements of polyaniline-based nanocomposites for supercapacitors, J. Power. Sources. 424 (2019) 108–130.

[15] Z. Yang, J. Ma, B. Bai, A. Qiu, D. Losic, D. Shi, M. Chen, Free-standing PEDOT/ polyaniline conductive polymer hydrogel for flexible solid-state supercapacitors, Electrochim. Acta 322 (2019) 134769.

[16] D. Xu, X. Xiao, J. Cai, J. Zhou, L. Zhang, Highly rate and cycling stable electrode materials constructed from polyaniline/cellulose nanoporous microspheres, J. Mater. Chem. A 3 (2015) 16424–16429.

[17] S.Shaheen Shah, S. Oladepo, M. Ali Ehsan, W. Iali, A. Alenaizan, M.Nahid Siddiqui, M. Oyama, A.R. Al-Betar, M.A. Aziz, Recent progress in polyaniline and its composites for supercapacitors, Chem. Rec. 24 (2024) e202300105.

[18] F. Kazemi, S. Naghib, Z. Mohammadpour, Multifunctional micro-/nanoscaled structures based on polyaniline: an overview of modern emerging devices, Mater. Today Chem. 16 (2020) 100249.

[19] A. Waheed, N. Baig, N. Ullah, W. Falath, Removal of hazardous dyes, toxic metal ions and organic pollutants from wastewater by using porous hyper-cross-linked polymeric materials: a review of recent advances, J. Environ. Manage 287 (2021) 112360.

[20] C. Zhang, S. Wang, Z. Zhan, A.M. Amin, B. Tan, Synthesis of MWCNT-based hyper-cross-linked polymers with thickness-tunable organic porous layers, ACS Macro Lett. 8 (2019) 403–408.

[21] P. Liu, Q. Liao, T. Zhao, W. Xiong, F. Liu, X. Hu, Implantation of guanidine chemical adsorption sites in hyper-crosslinked polymers for effective adsorption and conversion of H2S, Chem. Eng. J. 487 (2024) 150481.

[22] L. Tan, B. Tan, Hypercrosslinked porous polymer materials: design, synthesis, and applications, Chem. Soc. Rev. 46 (2017) 3322–3356.

[23] L. Ding, H. Gao, F. Xie, W. Li, H. Bai, L. Li, Porosity-enhanced polymers from hyper-cross-linked polymer precursors, Macromolecules 50 (2017) 956–962.

[24] M.G. Mohamed, A.F.M. EL-Mahdy, M.G. Kotp, S.-W. Kuo, Advances in porous organic polymers: syntheses, structures, and diverse applications, Mater. Adv. 3 (2022) 707–733, https://doi.org/10.1039/D1MA00771H.

[25] C. Zhang, R. Kong, X. Wang, Y. Xu, F. Wang, W. Ren, Y. Wang, F. Su, J.-X. Jiang, Porous carbons derived from hypercrosslinked porous polymers for gas adsorption and energy storage, Carbon 114 (2017) 608–618.

[26] B. Zheng, X. Lin, X. Zhang, D. Wu, K. Matyjaszewski, Emerging functional porous polymeric and carbonaceous materials for environmental treatment and energy storage, Adv. Funct. Mater. 30 (2020) 1907006.

[27] L. Tan, B. Tan, Functionalized hierarchical porous polymeric monoliths as versatile platforms to support uniform and ultrafine metal nanoparticles for heterogeneous catalysis, Chem. Eng. J. 390 (2020) 124485.

[28] A.F.M. EL-Mahdy, A.M. Elewa, S.W. Huang, H.H. Chou, S.W. Kuo, Dual-function fluorescent covalent organic frameworks: HCl sensing and photocatalytic H2 evolution from water, Adv. Opt. Mater. 8 (2020) 2000641, https://doi.org/10.1002/adom.202000641.

[29] B. Zhang, W. Wang, L. Liang, Z. Xu, X. Li, S. Qiao, Prevailing conjugated porous polymers for electrochemical energy storage and conversion: lithium-ion batteries, supercapacitors and water-splitting, Coord. Chem. Rev. 436 (2021) 213782.

[30] L. Peng, Y. Cai, Y. Luo, G. Yuan, J. Huang, C. Hu, H. Dong, Y. Xiao, Y. Liang, Y. Liu, Bioinspired highly crumpled porous carbons with multidirectional porosity for high rate performance electrochemical supercapacitors, ACS Sustain. Chem. Eng. ACS 6 (2018) 12716–12726.

[31] M.G. Mohamed, C.-C. Lee, A.F.M. EL-Mahdy, J. Lüder, M.-H. Yu, Z. Li, Z. Zhu, C.-C. Chueh, S.-W. Kuo, Exploitation of two-dimensional conjugated covalent organic frameworks based on tetraphenylethylene with bicarbazole and pyrene units and applications in perovskite solar cells, J. Mater. Chem. A 8 (2020) 11448–11459, https://doi.org/10.1039/D0TA02956D.

[32] M.G. Kotp, N.L. Torad, H. Nara, W. Chaikittisilp, J. You, Y. Yamauchi, A.F.M. EL-Mahdy, S.-W. Kuo, Tunable thiophene-based conjugated microporous polymers for the disposal of toxic hexavalent chromium, J. Mater. Chem. A 11 (2023) 15022–15032.

[33] M.G. Kotp, N.L. Torad, J. Lüder, A. El-Amir, W. Chaikittisilp, Y. Yamauchi, A.F.M. EL-Mahdy, A phenazine conjugated microporous polymer-based quartz crystal microbalance for sensitive detection of formaldehyde vapors at room temperature:

an experiment and density functional theory study, J. Mater. Chem. A 11 (2023) 764–774, https://doi.org/10.1039/D2TA07966F.

[34] P. Dubey, V. Shrivastav, T. Boruah, G. Zoppellaro, R. Zbořil, A. Bakandritsos, S. Sundriyal, Unveiling the potential of covalent organic frameworks for energy storage: developments, challenges, and future prospects, Adv. Energy Mater. (2024) 2400521.

[35] A.M. Elewa, A.F.M. EL-Mahdy, M.H. Elsayed, M.G. Mohamed, S.-W. Kuo, H.-H. Chou, Sulfur-doped triazine-conjugated microporous polymers for achieving the robust visible-light-driven hydrogen evolution, Chem. Eng. J. 421 (2021) 129825, https://doi.org/10.1016/j.cej.2021.129825.

[36] M.G. Kotp, A.M. Elewa, A.F.M. EL-Mahdy, H.-H. Chou, S.-W. Kuo, Tunable pyridyl-based conjugated microporous polymers for visible light-driven hydrogen evolution, ACS Appl. Energy Mater. 4 (2021) 13140–13151, https://doi.org/10.1021/acsaem.1c02772.

[37] N.A. Mahynski, S.K. Kumar, A.Z. Panagiotopoulos, Relative stability of the FCC and HCP polymorphs with interacting polymers, Soft. Matter. 11 (2015) 280–289.

[38] V. Sudarsan, Materials Under Extreme Conditions, Elsevier, 2017, pp. 129–158.

[39] M.G. Kotp, S.-W. Kuo, Harnessing solar energy with porous organic polymers: advancements, challenges, economic, environmental impacts and future prospects in sustainable photocatalysis, Mater. Today Chem. 41 (2024) 102299.

[40] S. Millán-Martín, C. Jakes, S. Carillo, R. Rogers, D. Ren, J. Bones, Comprehensive multi-attribute method workflow for biotherapeutic characterization and current good manufacturing practices testing, Nat. Protoc. 18 (2023) 1056–1089.

[41] S. Muthu, J.U. Maheswari, Quantum mechanical study and spectroscopic (FT-IR, FT-Raman, 13C, 1H, UV) study, first order hyperpolarizability, NBO analysis, HOMO and LUMO analysis of 4-[(4-aminobenzene) sulfonyl] aniline by ab initio HF and density functional method, Spectrochim. Acta A 92 (2012) 154–163.

[42] S.J. Dünki, E. Cuervo-Reyes, D.M. Opris, A facile synthetic strategy to polysiloxanes containing sulfonyl side groups with high dielectric permittivity, Polym. Chem. 8 (2017) 715–724.

[43] A. Ulman, C.S. Willand, W. Kohler, D.R. Robello, D.J. Williams, L. Handley, New sulfonyl-containing materials for nonlinear optics: semiempirical calculations, synthesis, and properties, J. Am. Chem. Soc. 112 (1990) 7083–7090.

[44] H. Zhu, Y. Xie, Electrochemical performance of bridge molecule-reinforced activated carbon fiber-m-aminobenzenesulfonic acid-polyaniline for braidable-supercapacitor application, Chem. Eng. J. 478 (2023) 147416.

[45] M. Ayad, G. El-Hefnawy, S. Zaghlol, Facile synthesis of polyaniline nanoparticles; its adsorption behavior, Chem. Eng. J. 217 (2013) 460–465.

[46] M.M. Ayad, W.A. Amer, M.G. Kotp, I.M. Minisy, A.F. Rehab, D. Kopecký, P. Fitl, Synthesis of silver-anchored polyaniline–chitosan magnetic nanocomposite: a smart system for catalysis, RSC Adv. 7 (2017) 18553–18560, https://doi.org/10.1039/C7RA02575K.

[47] M.M. Ayad, W.A. Amer, M.G. Kotp, Magnetic polyaniline-chitosan nanocomposite decorated with palladium nanoparticles for enhanced catalytic reduction of 4-nitrophenol, Mol. Catal. 439 (2017) 72–80, https://doi.org/10.1016/j.mcat.2017.06.023.

[48] I.M. Minisy, N.A. Salahuddin, M.M. Ayad, Adsorption of methylene blue onto chitosan–montmorillonite/polyaniline nanocomposite, Appl. Clay. Sci. 203 (2021) 105993.

[49] J. Garcia-Martinez, D. Cazorla-Amoros, A. Linares-Solano, SO2− faujasite interaction: a study by in situ ftir and thermogravimetry, Langmuir 18 (2002) 9778–9782.

[50] M. Rusop, T. Soga, T. Jimbo, X-ray photoelectron spectroscopy studies on the bonding properties of oxygenated amorphous carbon nitride thin films synthesized by pulsed laser deposition at different substrate temperatures, J. Non-Cryst. Solids 351 (2005) 3738–3746.

[51] S. Wu, Z. Cui, F. He, Z. Bai, S. Zhu, X. Yang, Characterization of the surface film formed from carbon dioxide corrosion on N80 steel, Mater. Lett. 58 (2004) 1076–1081.

[52] E. Lewin, P.Å. Persson, M. Lattemann, M. Stüber, M. Gorgoi, A. Sandell, C. Ziebert, F. Schäfers, W. Braun, J. Halbritter, On the origin of a third spectral component of C1s XPS-spectra for nc-TiC/aC nanocomposite thin films, Surf. Coat. Technol. 202 (2008) 3563–3570.

[53] F.-W. Zeng, X.-X. Liu, D. Diamond, K.T. Lau, Humidity sensors based on polyaniline nanofibres, Sens. Actuators. B 143 (2010) 530–534.

[54] A. Matikainen, T. Nuutinen, T. Itkonen, S. Heinilehto, J. Puustinen, J. Hiltunen, J. Lappalainen, P. Karioja, P. Vahimaa, Atmospheric oxidation and carbon contamination of silver and its effect on surface-enhanced Raman spectroscopy (SERS), Sci. Rep. 6 (2016) 37192.

[55] M.G. Kotp, S.-W. Kuo, A.F.M. EL-Mahdy, Phenazine-based conjugated microporous polymers: influence of planarity and imine content on energy storage performance, Colloids. Surf. A. (2024) 133210.

[56] S. Roy, P. Panda, S. Barman, Electrospun highly porous carbon nitride-carbon nanofibers for high performance supercapacitor application, J. Energy Storage 91 (2024) 112007.

[57] S. Sarkar, V. Thangadurai, Critical current densities for high-performance all-solid-state Li-metal batteries: fundamentals, mechanisms, interfaces, materials, and applications, ACS Energy Lett. 7 (2022) 1492–1527.

[58] N. Zdolšek, R.P. Rocha, J. Krstić, T. Trtić-Petrović, B. Šljukić, J.L. Figueiredo, M. J. Vujković, Electrochemical investigation of ionic liquid-derived porous carbon materials for supercapacitors: pseudocapacitance versus electrical double layer, Electrochim. Acta 298 (2019) 541–551.

[59] T. Liu, Y. Li, Addressing the Achilles' heel of pseudocapacitive materials: long-term stability, InfoMat 2 (2020) 807–842.

[60] M. Ejaz, M.G. Mohamed, Y.-T. Chen, K. Zhang, S.-W. Kuo, Porous carbon materials augmented with heteroatoms derived from hyperbranched biobased benzoxazine resins for enhanced CO2 adsorption and exceptional supercapacitor performance, J. Energy Storage 78 (2024) 110166.

[61] J. Zhao, A.F. Burke, Review on supercapacitors: technologies and performance evaluation, J. Energy Chem. 59 (2021) 276–291.